High-frequency dynamics of hybrid oxide Josephson heterostructures

P. Komissinskiy,[1,2,3,*] G. A. Ovsyannikov,[1,2] K. Y. Constantinian,[2] Y. V. Kislinski,[2] I. V. Borisenko,[2] I. I. Soloviev,[4] V. K. Kornev,[4] E. Goldobin,[5] and D. Winkler[1]

[1]*Department of Microtechnology and Nanoscience, Chalmers University of Technology, SE-41296, Göteborg, Sweden*

[2]*Institute of Radio Engineering and Electronics, Russian Academy of Sciences, 125009, Moscow, Russia*

[3]*Institut für Materialwissenschaft, Technische Universität Darmstadt, Petersenstraße 23, 64287 Darmstadt, Germany*

[4]*Physics Department, Moscow State University, 119992 Moscow, Russia*

[5]*Physikalisches Institut-Experimentalphysik II, Universität Tübingen, Auf der Morgenstelle 14, D-72076 Tübingen, Germany*

(Received 28 November 2007; revised manuscript received 29 April 2008; published 1 July 2008)

We summarize our results on Josephson heterostructures Nb/Au/$YBa_2Cu_3O_x$ that combine conventional (S) and oxide high-T_c superconductors with a dominant *d*-wave symmetry of the superconducting order parameter (D). The heterostructures were fabricated on (001) and (1 1 20) $YBa_2Cu_3O_x$ films grown by pulsed laser deposition. The structural and surface studies of the (1 1 20) $YBa_2Cu_3O_x$ thin films reveal nanofaceted surface structure with two facet domain orientations, which are attributed as (001) and (110)-oriented surfaces of $YBa_2Cu_3O_x$ and result in $S/D_{(001)}$ and $S/D_{(110)}$ nanojunctions formed on the facets. Electrophysical properties of the Nb/Au/$YBa_2Cu_3O_x$ heterostructures are investigated by the electrical and magnetic measurements at low temperatures and analyzed within the faceting scenario. The superconducting current-phase relation (CPR) of the heterostructures with finite first and second harmonics is derived from the Shapiro steps, which appear in the *I-V* curves of the heterostructures irradiated at frequencies up to 100 GHz. The experimental positions and amplitudes of the Shapiro steps are explained within the modified resistive Josephson junction model, where the second harmonic of the CPR and capacitance of the Josephson junctions are taken into account. We experimentally observe a crossover from a lumped to a distributed Josephson junction limit for the size of the heterostructures smaller than Josephson penetration depth. The effect is attributed to the variations of the harmonics of the superconducting CPR across the heterojunction, which may give rise to splintered vortices of magnetic flux quantum. Our investigations of parameters and phenomena that are specific for superconductors having *d*-wave symmetry of the superconducting order parameter may be of importance for applications such as high-frequency detectors and novel elements of a possible quantum computer.

DOI: 10.1103/PhysRevB.78.024501 PACS number(s): 74.50.+r, 74.78.Fk, 74.45.+c

I. INTRODUCTION

During recent years the superconductors with dominating $d_{x^2-y^2}$-wave (*d*-wave) symmetry of the order parameter (denoted D in this paper) have received a lot of interest from the scientific community as a specific class of superconducting materials, which is significantly different from conventional *s*-wave superconductors (S) with an isotropic superconducting order parameter. The lobes of the *d*-wave superconducting order parameter are locked to the crystal lattice direction *a* and *b* and have opposite sign along the *a* and *b* axes (Fig. 1). At the moment there is experimental evidence that *d*-wave symmetry of the superconducting order parameter is the predominant one in oxide high-T_c superconductors.[1–3]

A phase difference φ equal to π in the ground state of the superconducting current-phase relation (CPR) $I_s(\varphi)$ may be observed in Josephson junctions (JJs) based on D superconductors integrated in superconducting loop.[4] These junctions are called π junctions in contrast to the "classical" JJs with zero phase difference $\varphi=0$ in the ground state (0 junctions).[4] The phase shift of π in the π JJ can be used as a phase shifter in rapid single-flux quantum logic circuits[4–6] and flux qubits.[7,8] A superconducting quantum interference device with π JJ (π-SQUID) was used to prove a dominant *d*-wave symmetry of the order parameter in oxide high-T_c superconductors.[2,3] A set of 0 and π junctions can be fabricated, for instance, in hybrid S/D JJs with the barrier situated between *a*- and *b*-oriented surfaces of high-T_c superconductor and an *s*-wave superconducting counter electrode.[9]

The *d*-wave symmetry of the superconducting order parameter may result in a nonsinusoidal CPR, in particular, in $S/D_{(110)}$ and $S/D_{(001)}$ JJs fabricated on the (110) and (001) surfaces of a D-superconducting crystal, respectively (see Fig. 1).[7,10] According to theoretical calculations[10–12] the CPR in S/D JJs contains first (I_{c1}), second (I_{c2}), etc. harmonics, i.e.,

$$I_s(\varphi) = I_{c1} \sin \varphi + I_{c2} \sin 2\varphi. \quad (1)$$

In this case the nonsinusoidal CPR of the JJ is characterized by $q \equiv \pm I_{c2}/I_{c1}$. If the amplitude of the second har-

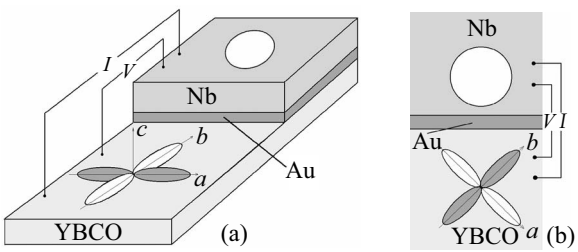

FIG. 1. Schematic diagram of the *I-V* curve measurements of the Nb/Au/YBCO JHSs in (a) $S/D_{(001)}$ and (b) $S/D_{(110)}$ geometry. *d*-wave and *s*-wave superconducting order parameters are shown in the YBCO and Nb electrodes, respectively.

monic of the CPR is negative and large enough, i.e., $q<-0.5$, then the phase difference $\varphi_0(q)$ in the ground state of the JJ is not zero and it satisfies the condition $0<\varphi_0<\pi/2$. We call such JJs φ_0 junctions in a similar manner to the above mentioned π junctions.[7,13,14] It is worth mentioning that the presence of nodal low-energy excitations in the spectrum of the JJs based on D superconductors does not change the junction's quantum state, i.e., one can observe macroscopic quantum tunneling in such a *d*-wave JJ.[8] Thus, superconducting rings containing JJs with a D superconductor can be used for realization of "quiet qubits"—two-level quantum systems, where no external magnetic-field bias is required.[7,8]

Note that the shape of the CPR of the JJs (in particular the amplitude of the second harmonic) may be affected by the low energy Andreev bound states, which manifest themselves as a conductance peak at zero voltage observed in $N/D_{(110)}$ (N is the normal metal), as well as in $S/D_{(110)}$ and $D_{(100)}/D_{(110)}$ junctions.[7,12,15,16] The Andreev bound states are formed at the surfaces close to the (110) crystallographic planes of *d*-wave superconductors if quasiparticles experience a sequence of specular and Andreev reflections with an additional phase shift caused by a sign change of the *d*-wave superconducting order parameter. Nonsinusoidal superconducting CPR was observed in asymmetrical YBCO bicrystal JJs,[2,17–20] hybrid $S/D_{(001)}$ thin film $Nb/Au/YBa_2Cu_3O_x$ (YBCO) Josephson heterostructures,[21,22] and hybrid $Nb/Au/Ca_{1-x}Sr_xCuO_2/YBCO$ thin-film Josephson heterojunctions with an antiferromagnetic layer.[23] A quantitative analysis of the experimentally observed second harmonic of the CPR is given in Ref. 21 in terms of the Au/YBCO interface transparency and predominant *d*-wave symmetry of the YBCO superconducting order parameter. The experimentally obtained nonzero first harmonic of the CPR is attributed to the influence of the admixed *s*-wave component of the superconducting order parameter of YBCO.[24–26]

Due to three-dimensional (3D) growth of high-T_c thin films, the surface roughness is larger than the interatomic distances, and faceting of the S/D and D/D interfaces occurs.[2] For instance, well-pronounced faceting takes place in YBCO bicrystal JJs, where the facets at a grain boundary are misoriented with respect to each other in the *ab* plane of YBCO. Because of the faceting, pairs of 0 and π nanojunctions are formed, which is equivalent to a superconducting critical current density $j_c(x)$ alternating along the bicrystal grain boundary.[2,27,28] As a result, a large negative second harmonic arises in the CPR of the bicrystal JJs and so-called splintered vortices are formed in the JJs.[27] A pair of splintered vortices carry magnetic fluxes $\Phi_1<\Phi_0/2$ and $\Phi_2>\Phi_0/2$, such that $\Phi_1+\Phi_2=\Phi_0$, ($\Phi_0=h/2e$ is the magnetic flux quantum, h is the Planck constant).[27] The splintered vortices have been experimentally observed in YBCO bicrystal JJs with a $D_{(100)}/D_{(110)}$ interface.[28] Vortices with fractions of flux quantum Φ_0 were observed in JJs made of conventional *s*-wave superconductors having either artificial phase discontinuities[28,29] or steplike variation of thickness of a ferromagnetic interlayer.[30]

In order to determine the CPR, the JJs of interest can be incorporated into a superconducting ring forming a dc (Refs. 19 and 20) or rf (Refs. 2, 17, 18, and 21) SQUID. In the latter case the rf SQUID was inductively coupled to a tank resonance circuit, and the rf impedance of the system was measured versus the external magnetic flux. Such a measurement technique works properly only in the nonhysteretic mode of the rf SQUID, restricting the critical current of the JJ to a very small value of a few μA. Thus, the technique of CPR measurement is not applicable for JJs with high critical-current density.

In the present work we report on experimental studies of the high-frequency properties of Nb/Au/YBCO μm-size Josephson mesa-heterostructures (JHSs). This technique imposes no constraints on the critical current of the JJ. The JHSs investigated here are fabricated using YBCO thin films grown on tilted substrates. The crystallographic *c* axis of the YBCO film is tilted with respect to the substrate normal direction as shown in Fig. 2(a). The fabrication and measurement techniques are discussed in Sec. II, where we also discuss the thin films surface morphology measurements using atomic force microscopy (AFM) and x-ray diffraction (XRD) analysis. Comparison with the JHSs fabricated using *c*-axis-oriented YBCO thin films is given. Section III presents electrical and magnetic measurements of the JHSs such as the *I-V* curves, temperature, and magnetic-field dependence of the critical current, $I_c(T)$ and $I_c(H)$, respectively. In particular, we discuss the influence of the second harmonic of the CPR on $I_c(H)$. Section IV is devoted to the microwave experiments, where the high frequency properties of the JHSs are presented and analyzed taking into account the junction capacitance and second harmonic of the CPR. We show the dependences of the integer and fractional Shapiro step amplitudes versus the applied microwave power and junction area. The obtained experimental results are discussed in Sec. V of the paper in the framework of the JHS model as an array of S/D nanojunctions with different CPRs. Summary of the obtained results is given in Sec. VI.

II. EXPERIMENTAL TECHNIQUES

A. Fabrication process

In order to fabricate S/D JHSs (001)- and (1 1 20)-oriented YBCO films were grown on top of (110)- and (7 10 2)-oriented $NdGaO_3$ substrates, respectively. The crystallographic *c* axis of the YBCO film on top of the (7 10 2) $NdGaO_3$ substrate is rotated in the (110) YBCO plane by approximately 11° with respect to the normal to the substrate plane. The orientation of the YBCO film is close to (1 1 20) as shown in Fig. 2(a). Epitaxial 150-nm-thick YBCO films were grown using pulsed laser deposition or dc sputtering techniques in oxygen atmosphere. Typical YBCO deposition rates were 30 nm/min for pulsed laser deposition and 1 nm/min for sputtering. All YBCO thin films have superconducting critical temperature $T_c>87$ K and the width of the superconducting transition $T_c<2$ K, determined using an inductive technique. 20 μm-long and 4 μm-wide microbridges parallel to the substrate edges {to the [20 0 1] and [0 20 1] YBCO directions of the (1 1 20)YBCO films, and to the [100] and [010] YBCO directions of the (001)YBCO films} were used to measure the critical current density in the YBCO films. At $T=77$ K the critical current densities of the

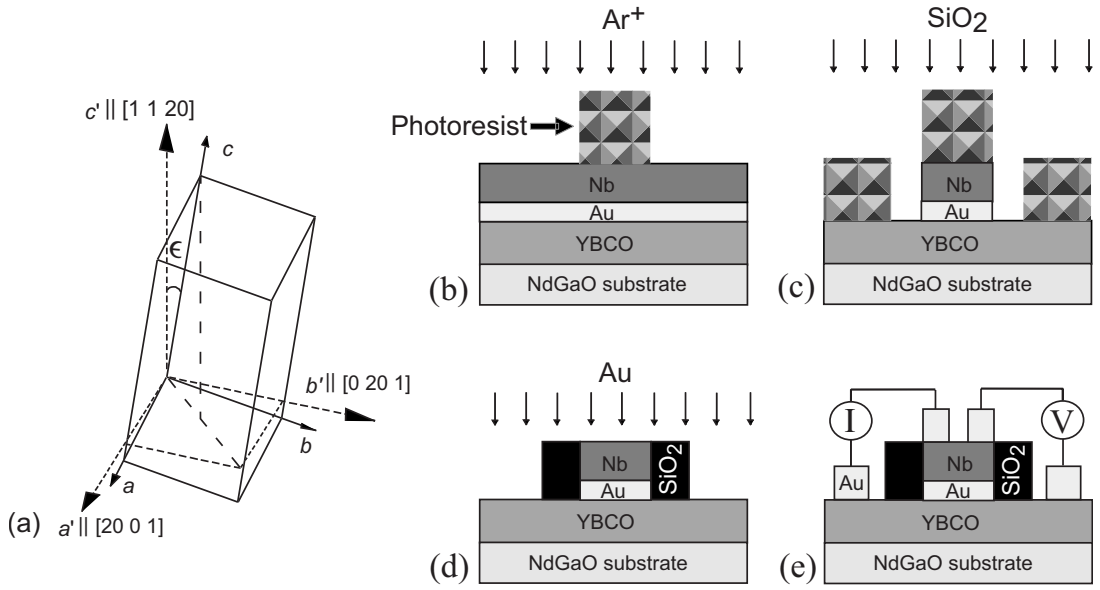

FIG. 2. (a) Crystallographic orientation of a (1 1 20) YBCO film grown on a (7 10 2) $NdGaO_3$ substrate. The rotation angles of the a, b, and c crystallographic axes of the (1 1 20) YBCO film with respect to the a', b', and c' axes of the standard (001)-oriented YBCO film on the (110) $NdGaO_3$ substrate are $\widehat{aa'}=7.6°$, $\widehat{bb'}=7.9°$, and $\epsilon=\widehat{cc'}=11°$. JHSs made with the (1 1 20) YBCO films are referred to in the text as t-JHSs. Sketch of the Nb/Au/YBCO JHS fabrication process: (b) Growth of epitaxial YBCO film by pulsed laser ablation, Au and Nb films by magnetron sputtering; photolithography and ion beam milling of the mesa; (c) deposition of interlayer insulation of SiO_2 film and liftoff; (d) deposition of extra Au films for JHS wiring; (e) JHS geometry and used measurement scheme.

microbridges of the (1 1 20) YBCO films are $j_c[20\ 0\ 1]=7.5\cdot10^4$ and $j_c[0\ 20\ 1]=2.0\cdot10^4$ A/cm^2, while we obtained $j_c^{ab}\approx10^6$ A/cm^2 for any arbitrary orientation of the microbridges in the ab planes of the (001) YBCO films. Since the critical current density of the JHSs is significantly smaller than j_c of the YBCO films, we can neglect depairing effects in YBCO superconducting counter electrode of the JHSs.

The Nb/Au/YBCO JHS fabrication procedure is shown in Figs. 2(b)–2(e). The deposited YBCO film was *in situ* coated with a 10-nm-thick Au film immediately after cooling down to room temperature. Additional Au and Nb layers were deposited in other vacuum chambers by electron-beam evaporation and rf magnetron sputtering, respectively. Thus, the Nb/Au/YBCO trilayer structure is formed [Fig. 2(b)]. The square JHSs with side L, varied from 5 to 50 μm, were produced using photolithography and argon ion-beam milling. An insulating SiO_2 layer was deposited by electron-beam technique. It allows to localize the area of current flow and to prevent undesirable contacts at the edges of the YBCO layer [Fig. 2(c)]. A 200-nm-thick Au film was deposited on top of the JHS and patterned in order to wire the JHS [Figs. 2(d) and 2(e)]. From 5 to 20 JHSs were usually fabricated on a 5×5 mm^2 chip. More details of the fabrication process have been published elsewhere.[16,21,22]

The dc parameters of the JHSs were measured in the current-biased regime using a three-point scheme in the temperature range $T=4.2-300$ K and magnetic fields up to 5 T [see Fig. 2(e)]. At $T<T_c$ the used measurement currents were smaller than the superconducting critical currents of the YBCO electrodes. Thus, at $T<T_c$ the YBCO electrodes were superconducting and did not contribute to the measurements resulting in an effective four-point measurement scheme. For the investigation of dynamic properties at frequencies $f_e=40-100$ GHz, the JHSs were incorporated into log-periodic antennas (Fig. 3).

The results of dc measurements at $T=4.2$ K are listed in Table I, where the parameters are reported for the JHSs on (001) YBCO films (c-JHS) and for the JHS on (1 1 20) YBCO films with tilted c axis (t-JHS). The data are presented for five t-JHSs of different sizes fabricated on the same chip. Two reported c-JHSs were fabricated on (110) $NdGaO_3$ substrate. The spread of the JHSs' parameters on different chips may be related to an intermediate layer at the Au/YBCO interface, where oxygen content fluctuates even with the minor differences in the fabrication process. However, qualitatively the dc properties of the JHSs are reproducible from one chip to another.

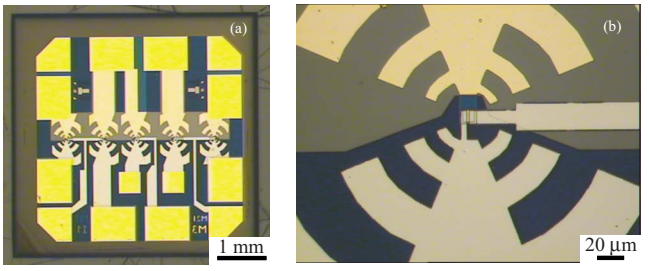

FIG. 3. (Color online) (a) Optical image of the 5×5 mm^2 chip containing five JHSs integrated into log-periodic antennas. Different wiring is used for dc and high-frequency electrical currents; (b) High-magnification optical image of a 20×20 μm JHS. The current leads realizing four-point measurement at $T<T_c$ are shown besides log-periodic antenna.

TABLE I. Parameters of the investigated Nb/Au/YBCO JHSs at $T=4.2$ K and $H=0$. The *t*-JHSs #1 – #5 were fabricated on the same chip. Parameters L, I_c, and R_N are the linear size, superconducting critical current, and normal resistance of the JHSs, respectively. Values of Josephson penetration depth λ_J were calculated from the critical current density using Eq. (9). JHSs capacitance is characterized by McCumber parameter $\beta \equiv 2\pi I_c R_N^2 C/\Phi_0$ calculated from hysteresis of the JHSs *I-V* curves. A ratio between amplitudes of the first and second harmonics of superconducting current-phase relation $|q|$ was obtained from the analysis of the experimentally observed integer Shapiro steps as described in Sec. IV B.

Sample #	ϵ (deg)	L (μm)	I_c (μA)	R_N (Ω)	I_cR_N (μV)	λ_J (μm)	β	$\|q\|$
t-JHS #1	11	50	198	0.44	87	120	6	
t-JHS #2	11	40	161	0.36	58	100	6	0.9
t-JHS #3	11	30	60	0.93	56	130	3	0.3
t-JHS #4	11	20	20	3.6	72	150	4	0.14
t-JHS #5	11	10	15	6	90	90	1	
c-JHS #1	11	10	2	19	38	250	3	0.2
c-JHS #2	11	15	15	5.1	76	140	10	

B. X-ray diffraction analysis

Crystallographic properties of the obtained YBCO films on (110) and (7 10 2) $NdGaO_3$ substrates were studied by XRD analysis. The $NdGaO_3$ substrates have a perovskite orthorhombic crystal lattice with $a=0.543$ nm, $b=0.55$ nm, and $c=0.771$ nm. The YBCO thin films follow the epitaxial relations: $(001)YBCO \| (110)NdGaO_3$ and $[010]YBCO \| [001]NdGaO_3$.[31] Thus, (110) planes of the $NdGaO_3$ substrates are used as growth templates for *c*-axis-oriented YBCO films. If the $NdGaO_3$ substrate surface is tilted from the (110) plane (the inclined $NdGaO_3$ substrates), then the epitaxial relations above are preserved and the *c* axis of the grown YBCO film is tilted from the substrate normal.[32–34]

Along with (110) $NdGaO_3$ substrates we investigated (120), (130), and (7 10 2) $NdGaO_3$ substrates with the inclination angles $\epsilon=11-26°$. The inclination of the (120)- and (130)-oriented $NdGaO_3$ substrates from the (110) $NdGaO_3$ planes is realized as a rotation around the [001] $NdGaO_3$ direction; in order to obtain the (7 10 2) $NdGaO_3$ substrates, the (110) $NdGaO_3$ planes are rotated around [111] $NdGaO_3$. The accuracy of the substrate orientations was checked by XRD rocking curve scans and is better than 0.3°. The substrate surface was polished chemically and mechanically providing smooth surface (the peak-to-peak surface roughness was below 1 nm) suitable for epitaxial growth of YBCO films with perfect crystal structure.

Our XRD studies of the YBCO films deposited on $NdGaO_3$ substrates revealed their orthorhombic crystal structure with lattice parameters $a=0.382-0.383$ nm, $b=0.388-0.389$ nm, and $c=1.167-1.168$ nm. The YBCO thin films tend to grow according to the epitaxial relations mentioned above. This has been confirmed by our earlier XRD studies.[32,33] If the $NdGaO_3$ substrate is inclined from the (110) $NdGaO_3$, then two growth-domain orientations of the YBCO film are formed on two symmetrically equivalent (110) and $(1\bar{1}0)$ $NdGaO_3$ template planes.[32,33] In that case we denote one of the domains (with YBCO *c* axis close to the substrate normal direction) as pseudo-*c* oriented and the other one (with *c* axis close to the substrate plane) as pseudo-*a* oriented. Thermodynamic conditions for the domain formation are identical, so the volume ratio of different domain is determined by the kinetic factors during YBCO thin-film deposition process such as density of the thin-film nucleation centers and the preferential growth direction.

The ratio between the pseudo-*c*- and pseudo-*a*-oriented domains in the YBCO films correlates with the areas of the (110) and $(1\bar{1}0)$ template planes on the $NdGaO_3$ substrate surface and changes with ϵ. At small ϵ, the formation of pseudo-*a*-oriented domains is suppressed, but rapidly increases with ϵ. For the angles $\epsilon=15-20°$ the areas of the pseudo-*a*- and pseudo-*c*-oriented domains of the YBCO film become comparable.[32,33]

Twinning in the *ab* planes is usually observed in *c*-axis-oriented YBCO films. In the YBCO films grown on (110) $NdGaO_3$ substrates, it manifests itself in 2θ and θ splitting of the (h0l) XRD peaks because of the difference in the values of *a* and *b* lattice constants and their misorientation, respectively. The splitting of the (h0l) XRD peaks has been observed in our two-dimensional $\theta-2\theta$ XRD mappings of the YBCO films on (110) $NdGaO_3$ (Fig. 4). The presence of the four peaks in Fig. 4(a) indicates twinning along two symmetrical (110) and $(1\bar{1}0)$ planes of YBCO. The misorientation of some of the twin domains is clearly seen in Fig. 4(a) as a splitting of the XRD reflections relative to the $(2\theta)=2\times\theta$ dashed line.

For the vicinal $NdGaO_3$ substrates, the twinning is suppressed with an increase in ϵ. The inclination around the [111] axis of $NdGaO_3$ breaks the symmetry of the (110) and $(1\bar{1}0)$ twinning planes of the YBCO films. In the case of the (7 10 2) $NdGaO_3$ substrate, the 11° inclination around [111] $NdGaO_3$ preserves only one of the twinning directions of YBCO. Thus, we obtain only two peaks on the $\theta-2\theta$ diagram [Fig. 4(b)]. Inclination of the substrate surface around [001] $NdGaO_3$ by the small angle $\epsilon \approx 10°$ preserves both possible YBCO twinning planes. However with further increase in the inclination ($\epsilon > 15°$) around [001] $NdGaO_3$, the twinning is completely suppressed [Fig. 4(c)]. Note that even in the untwinned YBCO films on the substrates with large inclination angles, the volumes of pseudo-*c*- and pseudo-*a*-oriented domains are almost equal. XRD patterns

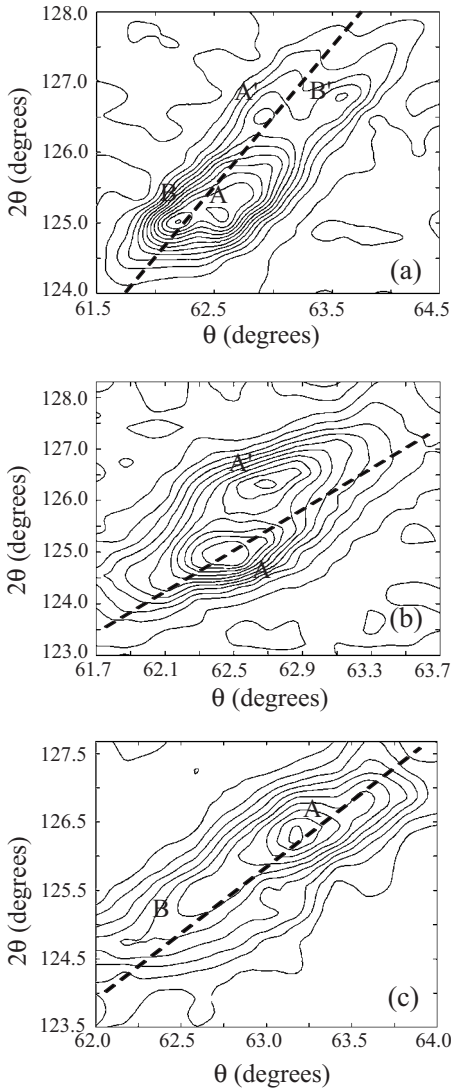

FIG. 4. Two-dimensional $\theta-2\theta$ x-ray diffraction spectral maps of (103) and (013) reflections of YBCO thin films on different $NdGaO_3$ substrates: (a) (110) $NdGaO_3$ substrate. The two twinning planes are (110) (A and A' peaks) and (1 $\bar{1}$ 0) (B and B' peaks); (b) (7 10 2) $NdGaO_3$ substrate. The A and A' peaks from the single (110) twinning plane are observed; (c) (130) $NdGaO_3$ substrate. One A peak is observed. No twinning occurs. $(2\theta)=2\times\theta$ dashed line is shown to indicate the splitting positions of the reflections.

of the YBCO films grown on the (7 10 2) $NdGaO_3$ substrates demonstrate that these films have only one growth domain (pseudo-c- and pseudo-a-oriented domains are degenerated) and one twin-domain complex, in contrast, for instance, to YBCO films on (110) $SrTiO_3$ or (120) $NdGaO_3$ substrates.[32–34]

C. Thin-film surface morphology

The morphology of the YBCO films was studied by AFM. TEM investigation presented in Ref. 35 demonstrates that Au/YBCO interface is atomically flat. For the c-oriented YBCO films a maximum peak-to-peak surface roughness of less than 3 nm was measured in approximately 100-nm-long surface islands of the YBCO growth [Figs. 5(a) and 5(b)].[36]

The surface of the (1 1 20) YBCO film in the t-JHSs on (7 10 2) $NdGaO_3$ substrates consists of large growth steps forming much longer and higher terraces than those on the substrate surface. Our AFM measurements show that the peak-to-peak surface roughness of the (1 1 20) YBCO film is 20 nm [Figs. 5(c) and 5(d)]. The longer and shorter sides of the growth steps are oriented preferably parallel to the (001) and (110) YBCO crystal planes, respectively, and show maximum peak-to-peak surface roughness of about one YBCO unit cell ($\approx$1 nm) (Ref. 16) [Figs. 5(c) and 5(d)]. The values of the root-mean-square surface roughness on (001) and (110) YBCO planes are equal to $\sigma_{(001)}\approx 0.6$ nm and $\sigma_{(110)}\approx 1.3$ nm, respectively. The interface itself can be considered as a sequence of (001) and (110) facets.[16,37,38] Therefore, the electrical current through the Au/YBCO interface on the tilted (1 1 20) YBCO film is a superposition of the currents flowing via the nanocontacts to the (001) and (110) crystallographic planes of YBCO. As it follows from Fig. 5, the height of the growth facets is equal to 15–20 nm and their length is approximately 300 nm.

Thus, in the t-JHS we have an array of parallel S/D nanojunctions between the S superconductor (Nb) and (001)- or (110)-oriented growth facets of the D superconductor ($S/D_{(001)}$ and $S/D_{(110)}$ nanojunctions, respectively). Superconducting and quasiparticle properties of the $S/D_{(001)}$ and $S/D_{(110)}$ nanojunctions are different because of YBCO thin-film anisotropy, including d-wave symmetry of the superconducting order parameter in the ab plane.

III. DC PROPERTIES OF THE JOSEPHSON HETEROSTRUCTURES

A. Resistance of the interfaces in the Josephson heterostructures

There are two important interfaces in the JHSs, namely, Nb/Au and Au/YBCO interfaces (see Fig. 3). Recalling the fact that the characteristic resistance r of the contact between two metals is determined by their Fermi momenta p_{F1} and p_{F2} (Refs. 39–41)

$$r=\frac{h^3}{4\pi e^2 p_{\min}^2}\frac{1}{2\bar{\mathfrak{I}}}, \tag{2}$$

where $p_{\min}=\min(p_{F1},p_{F2})$, $\bar{\mathfrak{I}}\equiv\langle\cos\alpha\mathfrak{I}(\alpha)\rangle$, $\mathfrak{I}(\alpha)$ is the interface transparency, where the averaging in $\langle\ldots\rangle$ is done over the direction angles; α is the angle between the quasiparticle momentum and the normal to the interface. In the case of an atomically flat and clean interface between two metals having spherical Fermi surfaces with Fermi velocities ϑ_{F1} and ϑ_{F2}, $\vartheta_{F1}\ll\vartheta_{F2}$, we obtain the following expressions for $\mathfrak{I}(\alpha)$ and $\bar{\mathfrak{I}}$:[40]

$$\mathfrak{I}(\alpha)=4\cos\alpha\vartheta_{F1}/\vartheta_{F2},\quad 2\langle\cos\alpha\mathfrak{I}(\alpha)\rangle=8\vartheta_{F1}/3\vartheta_{F2}. \tag{3}$$

From Eq. (3) it is clear that $\bar{\mathfrak{I}}\ll 1$ if $\vartheta_{F1}\ll\vartheta_{F2}$. If, however, the interface is rough in a scale of h/p_F then $\bar{\mathfrak{I}}\approx 1$ independently of the ratio between ϑ_{F1} and ϑ_{F2}.[40] Typically the normal resistance of the Nb/Au interface $R_{\mathrm{Nb/Au}}$ results in

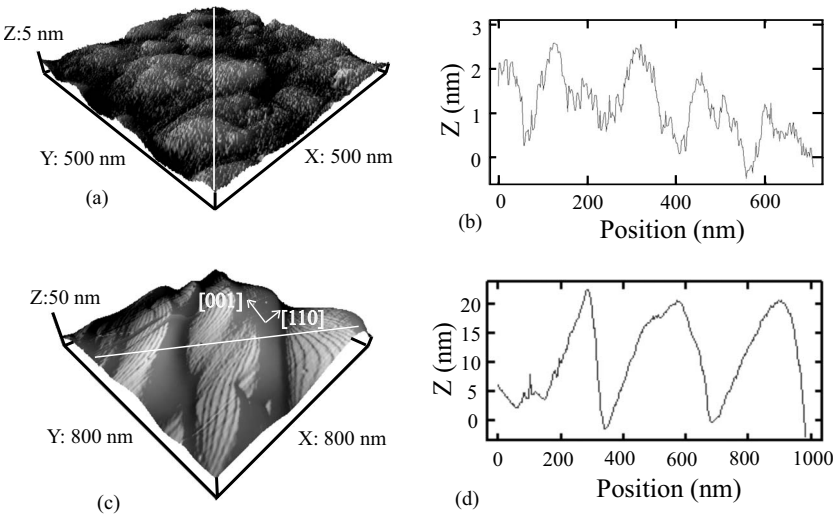

FIG. 5. 3D images of (a) *c* axis and (c) (1 1 20)-oriented YBCO-film surfaces obtained by using atomic force microscope. Cross-section graphs (b) and (d) show surface morphology of the *c* axis and (1 1 20)-oriented YBCO films along the white lines on (a) and (c), respectively. The longer and shorter sides of the (1 1 20) YBCO film facets in (b) and (d) demonstrate maximum peak-to-peak surface roughness below 1 nm.

$r_{\mathrm{Nb/Au}}=R_{\mathrm{Nb/Au}}L^2\sim 10^{-11}\ \Omega\times\mathrm{cm}^2$ and $\tilde{\mathfrak{I}}_{\mathrm{Nb/Au}}\approx 1$. The experimentally obtained characteristic resistance of the Nb/Au/YBCO JHS is equal to $r=R_NL^2\sim 10^{-5}-10^{-6}\ \Omega\times\mathrm{cm}^2$, where R_N is the normal resistance of the JHS, determined from the *I-V* curve of the JHS at $V>5$ mV. Thus, the Au/YBCO interface makes a decisive contribution to the JHS resistance.

The Au film between the Nb and YBCO layers prevents oxidation of Nb and oxygen depletion of the YBCO film surface. Our special investigations of the Nb/YBCO interface without Au layer in between the superconducting electrodes reveal much higher values of $r_{\mathrm{Nb/YBCO}}=0.1-1\ \Omega\times\mathrm{cm}^2$ and no superconducting current has been observed. If the Au layer is locally damaged because of the surface roughness of the YBCO film, then niobium oxide is locally formed at that point of the JHS and, thus, no microshort affecting the Josephson properties of the junction is possible due to the high resistance of the Nb/YBCO interface. Thus, deposition of an Au interlayer between Nb and YBCO electrodes is crucial for the experimental effects discussed in this paper. *S*-wave superconducting order parameter is induced in the Au layer as a result of the proximity effect between Au and *s*-wave superconductor (Nb) in the JHSs.

The anisotropy of Fermi momenta can be estimated using the value of p_F calculated as[42]

$$p_F^2=\frac{3h^3}{8\pi e^2\rho l}, \tag{4}$$

where ρ and l are the specific resistance and quasiparticle mean free path of the YBCO films. From our measurements of the *I-V* curves of the YBCO microbridges, we have determined the values of $\rho_c=2\cdot 10^{-1}\ \Omega\times\mathrm{cm}$ along the *c* axis and $\rho_{ab}=4\cdot 10^{-3}\ \Omega\times\mathrm{cm}$ in the *ab* plane of the YBCO films. Taking into account the l values along the *c* axis $l_c=1$ nm (Ref. 43) and in the *ab* plane $l_{ab}=10$ nm (Refs. 44 and 45) of YBCO we obtain $\rho_c l_c=2\cdot 10^{-8}\ \Omega\times\mathrm{cm}^2$, $\rho_{ab}l_{ab}=4\cdot 10^{-9}\ \Omega\times\mathrm{cm}^2$, and the ratio between the quasiparticle Fermi momenta in the *ab* plane and along *c* axis of YBCO is $p_{Fab}/p_{Fc}\approx 2.2$. Since this ratio is close to one, we can use isotropic Eqs. (2)–(4) for analyzing the current transport. When calculating the Au/YBCO interface transparency we should take into account the roughness of the YBCO surface facets [see Fig. 5]. Comparing the values of $\sigma_{(110)}\approx 1.3$ nm and $\sigma_{(001)}\approx 0.6$ nm determined in Sec. II C with the electron de Broglie wavelength of $\Lambda_{ab}=h/p_{Fab}\approx 12$ nm and $\Lambda_c=h/p_{Fc}\approx 25$ nm ($\sigma_{(110)}<\Lambda_{ab}$ and $\sigma_{(001)}<\Lambda_c$), respectively, we consider specular quasiparticle reflection at the Au/YBCO(001) and Au/YBCO(110) interfaces of the respective YBCO facets.[37–39]

In order to analyze possible contribution of the *ab*-plane YBCO facets (r_{ab}) in the current transport of the JHSs, we model the rough surface of YBCO as a parallel connection of the *ab*-plane and *c*-axis facets. For the *t*-JHSs we measure about one order of magnitude lower characteristic resistance (r_t) compared to the *c*-JHSs (r_c). For instance, $r_t\approx 2\ \mu\Omega\times\mathrm{cm}^2$ for the *t*-JHS #5 and $r_c\approx 19\ \mu\Omega\times\mathrm{cm}^2$ for the *c*-JHS #1 (see Table I). Thus, $r_t\ll r_c$ and we assume that in the *t*-JHSs, the current is transferred via the *ab*-plane facets, which are likely to be (110) oriented as it follows from the crystallographic and XRD measurements (see Sec. II). An independent proof of the dominant (110) YBCO transport channels in *t*-JHSs is the zero-bias conductance peak in their *I-V* curves (see Sec. III C).

Due to the peak-to-peak surface roughness of less than 3 nm between approximately 100 nm long islands of the (001)YBCO films in the *c*-JHSs, we expect more than 30 times larger contact area of the *c*-axis surfaces of the (001)YBCO films in comparison with the contact area of the exposed YBCO *ab*-plane surfaces (see Sec. II C). Thus, in the *c*-JHSs the contribution from the *ab*-plane transport channels is small. The experimentally evaluated average transparency of the *c*-JHS #1 is $2\tilde{\mathfrak{I}}_c\approx 7\cdot 10^{-4}\ll 1$, which is approximately two times lower than $2\tilde{\mathfrak{I}}_{(110)}\approx 1.3\cdot 10^{-3}\ll 1$ of the *t*-JHS #5. Thus, both *c*-JHSs and *t*-JHSs have average transparency inherent to tunnel junctions.

Note that Fig. 5 demonstrates the in-plane wavy surface of the (1 1 20) YBCO film with a characteristic length of approximately 100 nm in the direction parallel to the growth steps. This type of faceting originates from the island-type growth of the YBCO film and might be a source of additional in-plane faceting of the (1 1 20) YBCO film and result, for

instance, in current transport channels across (100)-oriented YBCO facets at the edges of the YBCO growth islands.

B. Superconducting current

The CPR of the JJs comprised of D superconductors depends strongly on the orientation of the *d*-wave order parameter with respect to the direction of the current transport. In particular, the CPR with only a second harmonic should be observed in $S/D_{(110)}$ and $S/D_{(001)}$ JJs,[10] and only a first harmonic should appear in the CPR of $S/D_{(100)}$ JJs. Both first and second harmonics should exist in the CPR of the JJs with an arbitrary oriented D superconductor. Earlier *c*-axis tunneling experiments with $S/D_{(001)}$ JJs have revealed a nonzero first harmonic of the CPR, which can be attributed to several possible mechanisms.[1] For instance, it might originate from the minor *s*-wave component of the superconducting order parameter in YBCO (Δ_s), which either may exist in YBCO,[26] arise at the YBCO surface,[46] or be generated across the twin boundaries,[47] and admixed to the dominant *d*-wave symmetrical component of the order parameter (Δ_d).

In that case it has been shown theoretically that in Nb/Au/YBCO $S/D_{(001)}$ JJs,[21]

$$I_{c1}R_N \approx \frac{\Delta_s \Delta_{\mathrm{Nb}}}{e\Delta_{\mathrm{D}}^*}, \tag{5}$$

$$I_{c2}R_N \approx \bar{\mathfrak{I}}\Delta_{\mathrm{Nb}}/e, \tag{6}$$

where Δ_{Nb} is the superconducting gap of Nb. In Eqs. (5) and (6) the superconducting order parameter of YBCO is described as a superposition of Δ_d and Δ_s: $\Delta(\varkappa)=\Delta_d \cos 2\varkappa + \Delta_s$, where $\varkappa$ is the angle between the quasiparticle momentum and the *a* axis of the YBCO film and[21]

$$\Delta_{\mathrm{D}}^* = \pi\Delta_d\left[2\ln\left(\frac{3.56\Delta_d}{k_B T_c^{\mathrm{Nb}}}\right)\right] \tag{7}$$

is valid under the assumption that $\Delta_d \gg \Delta_s$, Δ_{Nb} (T_c^{Nb} is a superconducting critical temperature of Nb and k_B is a Boltzmann constant).

Superconducting current with critical current density $j_c = 1-20$ A/cm^2 and $I_cR_N = 30-90$ μV is observed in the *I-V* curves of both *c*- and *t*-JHSs at $T=4.2$ K (see Table I). In accordance with Eq. (5), the experimental temperature dependence of the superconducting critical current $I_c(T)$ in the JHSs is similar to $\Delta_{\mathrm{Nb}}(T)$ determined from the *I-V* curves of the JHSs: the values of Δ_{Nb} and I_c vanish together at $T = 8.5-9.1$ K.[16,48] In our JHSs $\Delta_{\mathrm{Nb}}/e \approx \Delta_s/e \approx 1$ mV, $\Delta_d/e \approx 20$ mV, and the value of $I_cR_N \approx 100$ μV calculated by Eq. (5) correspond to the experimentally obtained values of I_cR_N in *c*-JHS (see Table I).

From the experimental values of r_c of the *c*-JHS we have calculated the value of the average transparency of the Au/YBCO interface as $\langle \cos\alpha \mathfrak{I}(\alpha)\rangle \approx 10^{-4}$. From Eqs. (5) and (6) it follows that the ratio between the second and first harmonics of the CPR is $|q| \approx \langle \cos\alpha \mathfrak{I}(\alpha)\rangle \Delta_{\mathrm{D}}^*/\Delta_s \approx 2\times 10^{-3}$. The experimentally measured higher values of $|q| \approx 0.1$, namely, the higher contribution of the second harmonic of the CPR in the *c*-JHSs,[16,22] might originate from the effects, which are not taken into account in the Eqs. (5) and (6): twinning of the YBCO films and fluctuations of the transparency across the junction area.[21] At the given values of $|q| \approx 0.1$, we have $I_c \approx I_{c1}$ and in the ground state of the JJ, $\varphi = 0$ (Fig. 6). Thus, the *c*-JHSs are "0-type" junctions. Note that no experimental observations of $|q| > 0.1$ in YBCO-based *c*-JHSs have been reported so far.

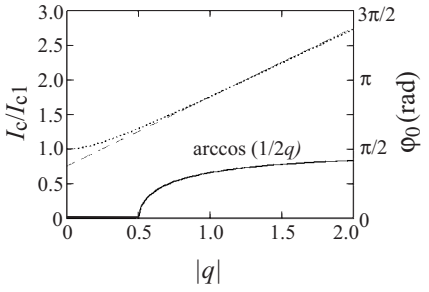

FIG. 6. Dependence of normalized critical current of the JJ, I_c/I_{c1} (dotted line), on the ratio between the amplitudes of the first (I_{c1}) and second (I_{c2}) harmonics of the superconducting CPR of the JJ $|q| \equiv I_{c2}/I_{c1}$. The asymptote of the $I_c/I_{c1}(q)$ dependence $I_c/I_{c1}(q\to\infty) = 1/\sqrt{2}+|q|$ is shown by the dash-dotted line. Phase stability of the JJ is characterized by the dependence of the phase difference in the ground state of the JJ φ_0 versus q (solid line).

Within the model of the dominant *d*-wave and small admixed *s*-wave component of the superconducting order parameter of YBCO, the first and second harmonics of the CPR in the $S/D_{(110)}$ JJs can also be described by Eqs. (1), (5), and (6). At low temperatures, the second harmonic of the CPR of the $S/D_{(110)}$ JJ can be enhanced up to $|q| \approx (\Delta_{\mathrm{D}}^*)^3\bar{\mathfrak{I}}/(\Delta_s\Delta_{\mathrm{Nb}}k_BT) \approx 0.8$ (Refs. 3 and 10–12) by the Andreev bound states at the (110) surfaces of YBCO. As a result the experimentally measured superconducting critical current is higher than the amplitude of the first harmonic of the CPR at $|q| \approx 0.1$, and the value of the phase difference in the ground state φ_0 is shifted from zero to $\varphi_0 \leq \pi/2$ (Fig. 6).[10–14]

The finite first harmonic of the CPR observed in the investigated JHSs might be alternatively explained by interface faceting in the *c*-JHSs, as well as in the $S/D_{(110)}$ and $S/D_{(001)}$ nanojunctions of the *t*-JHSs. As it has been demonstrated in Sec. III A this scenario is unlikely to be realized in the *c*-JHSs due to a small contribution of the *ab*-plane facets. The (1 1 20)YBCO film surface is atomically smooth in the $S/D_{(001)}$ and $S/D_{(110)}$ nanojunctions of the *t*-JHSs (see Fig. 5) and specular quasiparticle reflection occurs. The (100)-oriented YBCO facets in the *t*-JHSs mentioned in Sec. III A may, however, increase the amplitude of the first harmonic of the superconducting CPR in the *t*-JHSs. Although we are not able to distinguish between the two suggested scenarios of the finite first-harmonic generation in the CPR of the $S/D_{(110)}$ nanojunctions, they still can be considered as φ_0 junctions. The influence of the dominant *d*-wave superconducting order parameter on the CPR of the $S/D_{(110)}$ junction is similar to the case of YBCO bicrystal $D_{(100)}/D_{(110)}$ JJs where an unconventional CPR with large second harmonic has been experimentally demonstrated.[14,17–19]

C. Quasiparticle current

At low voltages $V < 1$ mV, the *I-V* curves of both types of the JHSs correspond to the resistive shunted junction

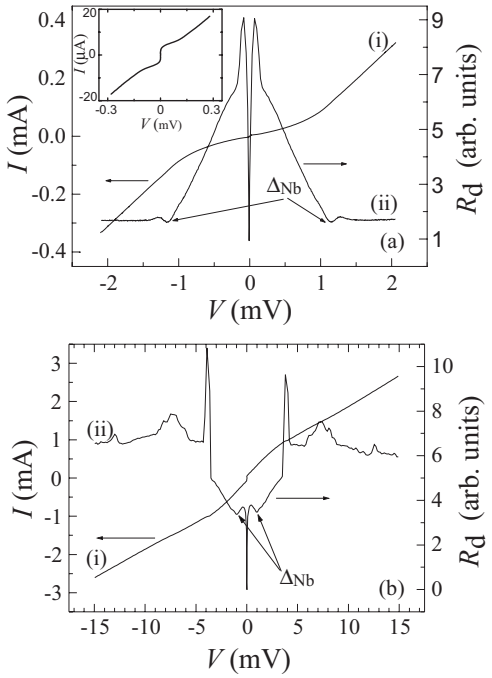

FIG. 7. The *I-V* curves (i) and differential resistance $R_d(V)$ dependences (ii) on the applied bias voltage for (a) *c*-JHS #1 ($L=10$ μm) and (b) *t*-JHS #5 ($L=10$ μm). The curves were measured at 4.2 K. The Nb superconducting gap is denoted as Δ_{Nb}. The peaks in the $R_d(V)$ dependence at $V>5$ mV [part (b)] are not discussed in the paper.

(RSJ) model of a JJ, where the capacitance C is taken into account through the McCumber parameter $\beta \equiv 2\pi I_c R_N^2 C/\Phi_0 = 0.5-5$.[49] The inset of Fig. 7(a) shows the *I-V* curve at $\beta<1$. The dependence of the differential resistance versus applied voltage $R_d(V)$ exhibits a local minimum at $V\approx 1.2$ mV as shown in Fig. 7(a). The position of the minimum coincides with Δ_{Nb}/e and has a temperature dependence close to the one given by the BCS theory. We note that previously a superconducting gap of an *s*-wave superconductor (Pb) was observed in the *c*-axis tunneling experiments in Pb/YBCO JHSs.[24,25] Significant peaks in $R_d(V)$, typical for a tunnel junction, has been observed at $|V|<\Delta_{Nb}/e$ (Fig. 7).[16] A sharp minimum of $R_d(V)$ at $|V|<0.3$ mV is attributed to the superconducting current (Fig. 7).

At the $S/D_{(110)}$ interfaces the quasiparticles undergo specular and Andreev reflections. If incident and Andreev-reflected quasiparticles experience a sign change of the *d*-wave superconducting order parameter, then a π shift is added to the phase of the quasiparticle wave function. In such case a sequence of mirror and Andreev quasiparticle reflections causes formation of Andreev bound states with low energies. As a result an anomalous zero bias conductance peak (ZBCP) should be observed in the *I-V* curves of $S/D_{(110)}$ ($N/D_{(110)}$) JJs.[3,15,16] ZBCP [a minimum of $R_d(V)$ dependence] has been routinely observed in the *I-V* curves of the *t*-JHSs at $V<4$ mV [Fig. 7(b)] in contrast to the *c*-JHSs, where no ZBCP has been found [Fig. 7(a)]. Thus, the observation of ZBCP is an independent indication of the dominant electrical current transport through (110) surfaces of the YBCO and points on the strong contribution of the $S/D_{(110)}$ nanojunctions to the electrical properties of the *t*-JHSs.

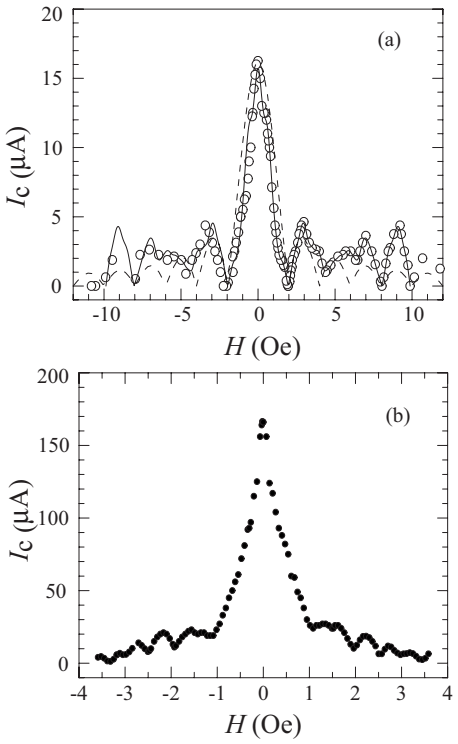

FIG. 8. (a) Dependence of critical current on the magnetic field $I_c(H)$ for the *t*-JHS #4 with $L=20$ μm (open circles). The related Fraunhofer dependence is shown by dashed line. The $I_c(H)$ curve calculated from the model of *t*-JHS consisting of arrays of the $S/D_{(001)}$ and $S/D_{(110)}$ nanojunctions (facets) connected in parallel is shown by the solid line; (b) $I_c(H)$ for the *t*-JHS #1 ($L=50$ μm). The condition $L<\lambda_J$ is fulfilled in both JHSs: $L=20$ and 50 μm, $\lambda_J=150$ and 120 μm, respectively. $T=4.2$ K.

D. Magnetic-field dependence of the critical current

We have traced changes in the experimental magnetic-field dependences $I_c(H)$ versus size of the *t*-JHSs. The $I_c(H)$ dependence for the *t*-JHS of $L=20$ μm looks similar to the Fraunhofer dependence $|\sin H|/H$,[50] which is observed in JJs with $L\lesssim\lambda_J$. This is shown in Fig. 8(a) by the dashed line. A small deviation of the $I_c(H)$ from $|\sin H|/H$ is observed in the vicinity of the central maximum ($H<1$ Oe). The deviation is increased in stronger magnetic fields indicating quasiuniform distribution of the superconducting current. It is possible to obtain a more precise approximation of the experimental dependence $I_c(H)$, especially in the range of high magnetic fields ($H>5$ Oe). We recall that our *t*-JHSs can be considered as arrays of 0 and φ_0 JJs, namely, $S/D_{(001)}$ and $S/D_{(110)}$ nanojunctions, respectively, connected in parallel and characterized by different ratios between the first and second harmonics of the superconducting CPR. Within such model we can calculate $I_c(H)$ using the following equation:[50]

$$I_c(H) = \max_{\delta\varphi}\left[\sum_{k=1}^{N} I_{c1}\frac{\sin(\pi x_k/L)}{\pi x_k/L}\sin(2\pi x_k/L + \delta\varphi) + \sum_{k=1}^{N} I_{c2}\frac{\sin(2\pi x_k/L)}{2\pi x_k/L}\sin(4\pi x_k/L + 2\delta\varphi)\right], \quad (8)$$

where $I_{c1}^{(k)}$ and $I_{c2}^{(k)}$ are the critical currents of the first and second harmonic of the CPR for the k-th nanojunction of the size x_k. Taking into account quasiperiodic distribution of the $S/D_{(001)}$ and $S/D_{(110)}$ nanojunctions across the t-JHS area with a period of 0.3 μm [see Figs. 5(c) and 5(d)], the experimental $I_c(H)$ dependence was fitted by this model. The following ratios between the harmonics of the superconducting CPR in the nanojunctions $I_{c1}^{(001)}/I_{c1}^{(110)}=3.3$ and $I_{c2}^{(001)}/I_{c2}^{(110)}=0.023$ were used in the fitting following the ratio between (001) and (110) YBCO surface facets in t-JHSs. In general, there is no unique solution of Eq. (8), and distribution of $S/D_{(001)}$ and $S/D_{(110)}$ nanojunctions across the t-JHS area cannot be unambiguously determined from the experimental $I_c(H)$ dependence. Similar models for the arrays of 0 and π JJs have been used in Refs. 9 and 51.

Following the experimental data (see Table I) the condition of lumped JJ $L<4\lambda_J$ is still satisfied for the largest JHSs ($L=50$ μm). However in spite of the fact that the shape of the $I_c(H)$ dependences is similar to the Fraunhofer dependence ($|\sin H|/H$) for $L\leq 20$ μm, at larger L the $I_c(H)$ noticeably differs from the Fraunhofer shape typical for lumped JJs and is rather similar to the $I_c(H)$ dependence of distributed JJs [Fig. 8(b)].[50] Thus, the crossover from lumped junction to distributed one is observed in t-JHS at $L=30$ μm $<4\lambda_J$. The reason for that might be a presence of the 0 and φ_0 nanojunctions and will be discussed later.

Note that in experiment λ_J is usually calculated from the average density of the superconducting critical current over JJ area $j_c=I_c/L^2$ as

$$\lambda_J^2 = \frac{\Phi_0}{2\pi\mu_0 d_{\text{eff}} j_c}, \quad (9)$$

where $d_{\text{eff}}=\lambda_{\text{Nb}}+\lambda_{\text{YBCO}}+d_{\text{Au}}+\chi$, $\lambda_{\text{Nb}}=70$ nm and $\lambda_{\text{YBCO}}=140$ nm are London penetration depths for Nb and YBCO, d_{Au} and χ are the thicknesses of the Au film and disordered interlayer (barrier) at the Au/YBCO interface, respectively, and d_{Au}, $\chi \ll \lambda_{\text{Nb}}$, λ_{YBCO}. At $T=4.2$ K and $j_c=1-10$ A/cm^2, $\lambda_J=100-300$ μm, which is longer than the maximal linear size L of the investigated JHSs (see Table I).

IV. HIGH-FREQUENCY DYNAMICS OF THE JOSEPHSON HETEROSTRUCTURES

Dynamic parameters of JJs are determined from investigations of Shapiro steps, which arise in the I-V curves of the JJs irradiated by electromagnetic waves of frequency f_e.[25,50,52] The Shapiro steps are due to synchronization between Josephson oscillations in the junction and the external electromagnetic wave.

Figure 9 presents a set of I-V curves for the t-JHS #2 at $T=4.2$ K; the autonomous I-V curve and I-V curves with external monochromatic electromagnetic radiation at f_e

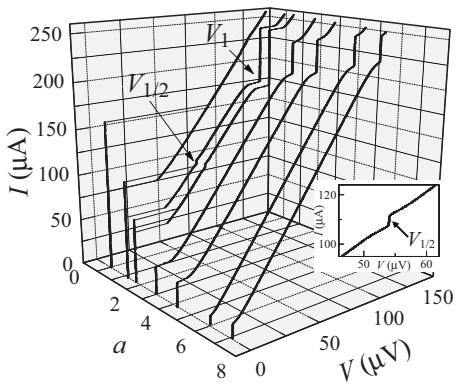

FIG. 9. I-V curves of t-JHS #2 ($L=40$ μm) versus normalized amplitude $a=i_{rf}/[\omega(\omega^2\beta^2+1)^{1/2}]$ of external electromagnetic waves at frequency $f_e=52$ GHz and temperature $T=4.2$ K. The autonomous I-V curve is given at $a=0$. The normalization coefficient $\omega(\omega^2\beta^2+1)^{1/2}=11.3$, where the McCumber parameter of the t-JHS, $\beta\approx 5$, was determined from the hysteresis in the autonomous I-V curve. Normalized frequency of the electromagnetic radiation is $\omega \approx f_e/f_c$, where $f_c=2\pi I_c R_N/\Phi_0$. Positions of the first harmonic ($V_1 \approx 108$ μV) and half-integer ($V_{1/2}\approx 54$ μV) Shapiro steps are shown. Inset: a detailed view of the half-integer Shapiro step $V_{1/2}$ ($a=1.2$).

$=52$ GHz. Integer Shapiro steps at voltages $V_k=k\Phi_0 f_e$ ($k=1,2\ldots$) and fractional Shapiro steps at $V_{1/2}=\Phi_0 f_e/2$ are visible in the I-V curves of irradiated t-JHSs; the steps at V_1 and $V_{1/2}$ are shown. The fractional Shapiro steps have been detected in the I-V curves of all measured t-JHSs irradiated in a broad frequency range (see inset Fig. 9). The fractional Shapiro steps may originate from the second harmonic of the superconducting CPR. On the other hand, fractional Shapiro steps may arise in the I-V curve due to the finite capacitance of the Josephson junction C, usually characterized by the McCumber parameter $\beta>1$.[49–53] The values of β in our t-JHSs, calculated from the hysteresis of the I-V curves, are below ten. In order to distinguish between the two factors we have studied amplitude dependences of the critical current I_c, first integer $I_1(k=1)$ and fractional (half integer) $I_{1/2}$ Shapiro steps versus the amplitude of the external electromagnetic wave I_{rf}. Based on our experimental data, we suggest a method to study dynamic properties of the JJs with unconventional superconducting CPR and finite junction capacitance ($\beta>1$).

A. Modified RSJ model for Josephson junctions with unconventional superconducting current-phase relation

We perform calculations of the amplitudes of the Shapiro steps based on a modified resistive shunted junction (MRSJ) model taking into account the second harmonic of the CPR, $|q|\neq 0$ and a finite capacitance of the JJs ($\beta>1$). Within the MRSJ, the basic equation of the JJ irradiated by external rf electromagnetic waves is written in normalized variables as

$$\beta\ddot{\varphi} + \dot{\varphi} + \sin\varphi + q\sin 2\varphi = i + i_{rf}\sin(\omega t) + i_f, \quad (10)$$

where $\omega=f_e/f_{c1}$ and $i_{rf}=I_{rf}/I_{c1}$ are the normalized frequency and amplitude of the external electromagnetic wave, f_{c1}

$=2\pi I_{c1}R_N/\Phi_0$ is the characteristic frequency of the Josephson oscillation used in Eq. (10) for normalization of time, $i=I/I_{c1}$ is the normalized bias current through the JJ, and $i_f=I_f/I_{c1}$ is the normalized current of thermal noise fluctuations.[49–53]

If one of the following conditions is satisfied (so-called high frequency limit)

$$\omega \gg 1, \quad \beta\omega^2 \gg 1, \quad i_{rf} \gg 1, \tag{11}$$

then the analytical solution of Eq. (10) can be found as a polynomial expansion. Indeed, the term $(\sin\varphi+q\sin 2\varphi)$ is small in comparison to the other components of Eq. (10) and can be used in a successive approximation technique. The analysis of contribution of the thermal noise fluctuations can be made only in case of large fluctuations ($i_f \gg 1$) by taking i_f into account in the first-order term of the successive approximation. Thus, the zero-order term of the successive approximation describes the autonomous *I-V* characteristic of the JJs. In case of negligible fluctuations ($i_f=0$), the first- and second-order terms of the approximation represent integer and fractional Shapiro steps in the *I-V* curves of the JJs, respectively.

B. Integer Shapiro steps

We emphasize that in case of negligible superconducting thermal noise fluctuations, our calculations using Eq. (10) ($i_f=0$) show that in the high-frequency limit the finite capacitance of the JJ does not change the amplitude values of the critical current $I_c(I_{rf})$ and harmonic Shapiro steps $I_n(I_{rf})$. However, there is a scaling of the argument from $a=i_{rf}/\omega$ for $\beta=0$ to $a=i_{rf}/[\omega(\omega^2\beta^2+1)^{1/2}]$ for $\beta>1$ in the $I_c(I_{rf})$ and $I_n(I_{rf})$ dependences. Thus at $q\neq 0$, the amplitudes of the critical current and integer Shapiro steps depend on a sum of the Bessel functions $J_n(a)$ with the modified arguments[52,53]

$$I_n/I_{c1} = 2\max_{\Theta}[J_n(a)\sin\Theta + qJ_{2n}(2a)\sin 2\Theta], \tag{12}$$

where the maximum of the expression in the square bracket is chosen depending on the shift of the phase Θ between Josephson and external oscillations.

The amplitude of the second harmonic of the CPR can be calculated from the experimental dependences $I_c(a)$ and $I_n(a)$ by fitting them with Eq. (12). For instance, at small values of $|q|$ the minimum of the critical current $I_c(a)$ is achieved at the values of $a=a_1$, where $J_0(a_1)\approx 0$, and the amplitude of I_{c2} can be derived from $q=I_{c2}/I_{c1}=I_c(a_1)/[I_c(0)J_0(2a_1)]$. For the experimental dependence of $I_c(a)$ for *t*-JHS #4 presented in Fig. 10(a), we obtain $|q|=0.14$, which is very close to $|q|=0.16$, calculated following the same procedure from the minimum of the first Shapiro step. In case of the larger JHSs ($L>20$ μm) higher minimum values of the $I_c(a)$ and $I_1(a)$ are observed experimentally, which correspond to the larger $|q|$. For the *t*-JHS #3 with $L=30$ μm, $|q|$ values of 0.43 and 0.34 are obtained from $I_c(a)$ and $I_1(a)$, respectively [Fig. 10(b)]. At even larger *t*-JHS #2 ($L>40$ μm), $|q|$ is increased to 0.9.

We assume that we can use the MRSJ model to analyze properties of both lumped and distributed JHSs although it is strictly applicable only for former ones. Thus, according to our analysis the experimentally observed changes in the $I_c(a)$ and $I_n(a)$ dependences for *t*-JHS with increasing L may originate from the increased contribution of the second harmonic component of the CPR. Normally $|q|$ should not depend on the junction length L.[50] A significant increase in the $|q|$ values of the *t*-JHSs correlates with a crossover from lumped to distributed regimes in $I_c(H)$ behavior (see Sec. III D). The increase in $|q|$ with L, which we observe for the *t*-JHSs, may be related to the fact that the lumped JJ model that we are using is not applicable for JHSs with $L>20$ μm. This is consistent with the fact that the $I_c(H)$ dependence deviates from the Fraunhofer pattern for $L>20$ μm. Note that only amplitudes but not the relative sign of the CPR harmonics can be derived from $I_c(a)$ and $I_n(a)$ dependences. In order to determine the relative sign of the CPR harmonics, an analysis of the fractional Shapiro steps is needed.

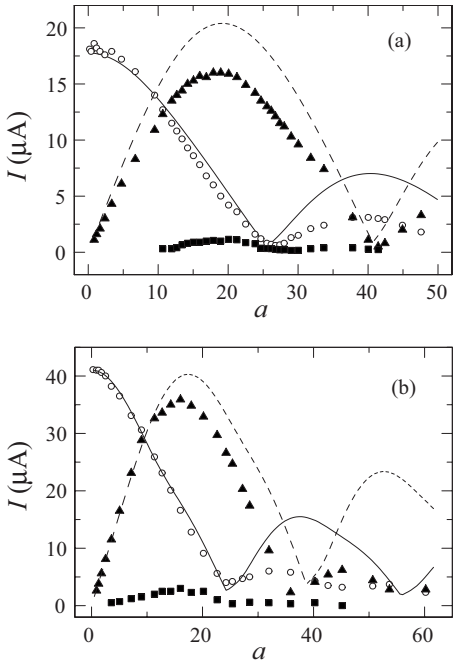

FIG. 10. Experimental dependences of the critical current (circles), the first harmonic (triangles) and half-integer (squares) Shapiro steps on the normalized amplitude of the microwave current $a=i_{rf}/[\omega(\omega^2\beta^2+1)^{1/2}]$. The experimental points are obtained at $T=4.2$ K. Solid and dashed lines are the results of the calculations using Eq. (12) for the critical current and the first Shapiro step, respectively. The data are presented for two experimental samples: (a) *t*-JHS #4 ($L=20$ μm), $\omega\approx 1.25$ and (b) *t*-JHS #3 ($L=30$ μm), $\omega\approx 1.8$. The best fits of the experimental $I_c(a)$ dependences were obtained at $|q|=0.14$ (*t*-JHS #4) and $|q|=0.43$ (*t*-JHS #3).

C. Fractional Shapiro steps

Presence of the second harmonic in the CPR of JJs and a large capacitance ($\beta>1$) promote fractional Shapiro steps like the one shown in inset of Fig. 9.[16,53,54] We observed fractional Shapiro steps at all frequencies of the external electromagnetic radiation. In the MRSJ model, both capaci-

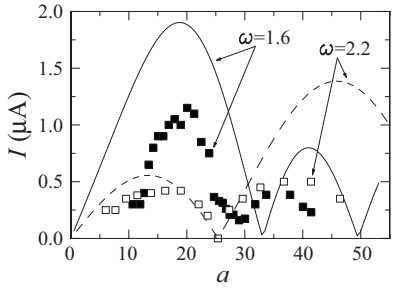

FIG. 11. Experimental dependences of half-integer $V_{1/2}$ Shapiro steps for t-JHS #4 (L=20 μm) on the amplitude of microwave current $a=I_{rf}/I_c$ for two normalized frequencies ω=1.6 and 2.2. The results of the calculations based on Eq. (13) are shown by the solid and dashed lines. The best fit of the experimental $I_{1/2}(a)$ dependences was obtained at q=−0.14, i.e., the first and second harmonics of the CPR of the t-JHS #4 have opposite signs.

tance and second harmonic of the CPR give rise to fractional Shapiro steps with the following amplitudes:[52,53]

$$I_{1/2}/I_c = 2 \max_{\Theta}\left\{ \sin\Theta\left[qJ_1(2a) + \beta\frac{J_1(a)J_0(a)}{(\beta\omega)^2/4+1} + 4q^2\beta\frac{J_2(2a)J_0(2a)}{(\beta\omega)^2+1}\cos\Theta\right]\right\}. \quad (13)$$

The maximum of the expression within the brackets is calculated depending on the phase shift Θ between Josephson and external oscillations. Using Eq. (13) we can calculate the values of $I_{1/2}(a)$ independently for positive and negative q and compare them with our experimental data. Our analysis presented in Fig. 11 points on negative q and, thus, on opposite signs of I_{c1} and I_{c2}, in the CPR of the JHSs. In fact, the amplitude of $I_{1/2}(a)$ calculated with $q>0$ is much larger than the experimental values and, in addition, does not have a local minimum experimentally observed between $a=0$ and $a=a_2$, where $I_c(a_2)=0$ [Fig. 10(a)]. The negative sign of q was theoretically predicted in $S/D_{(110)}$ JJs[11,14,18] and experimentally observed in $D_{(100)}/D_{(110)}$ YBCO bicrystal JJs.[18] At $\beta>1$ the sign of the part of Eq. (13) in the square brackets can be different depending on the contributions of the three terms of Eq. (13). Therefore, the $I_{1/2}(a)$ dependence for the JJ with $\beta>1$ might be different from the one for the JJs with $\beta=1$, where $I_{1/2}(a)\propto J_1(a)$. Note that small variations of the normalized frequency ω of the external electromagnetic radiation noticeably change the shape of the $I_{1/2}(a)$ dependence. This fact is connected to the simultaneous influence of the capacitance and second harmonic of the CPR on the $I_{1/2}(a)$ curve. The effect has been experimentally observed and fitted by making use of Eq. (13) for two normalized frequencies, although sometimes the maximal value of the experimental $I_{1/2}(a)$ is different from the results of the calculations. Note that no fitting parameters are used for comparison of our experimental data with the calculations (Fig. 11): a and q were derived from the $I_c(a)$ dependence, β was calculated from the autonomous I-V curve, and ω was extracted from frequency of external radiation.

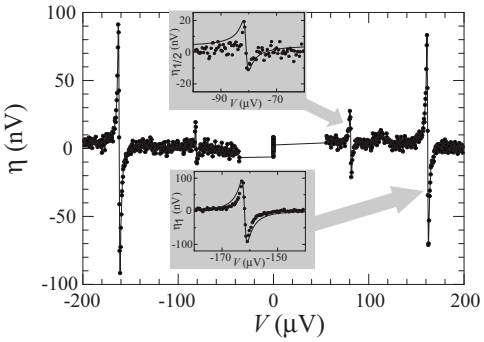

FIG. 12. Detector response of the t-JHS #2 (L=40 μm) measured at 78 GHz (ω=2.8). Insets present the detailed view of the (a) first integer and (b) half-integer features. Solid lines in insets (a) and (b) show fit of the experimentally measured detector response features by Eqs. (14) and (15), respectively.

D. Detector response of the Josephson heterostructures

The unconventional CPR and finite capacitance ($\beta>1$) of the JJ strongly influence the detector response of the JJ, $\eta \equiv \Delta V/V_0$, where ΔV is the voltage deviation of the I-V curve of the JJ irradiated by electromagnetic waves from the autonomous I-V curve.[50] Note that usually the detector response is introduced in case of a small amplitude of the external electromagnetic current (ΔV is a linear function of I_{rf}^2). In general, the resonance features of $\eta(V)$ should be observed in the detector response curve of the JJ near the voltages V_1 and $V_{1/2}$ of the first integer and half-integer Shapiro steps. Figure 12 shows the experimentally measured voltage dependence of the detector response of the t-JHS #2 at f_e=78 GHz. The amplitude of the detector response at $V_{1/2}$ is much smaller than that at V_1.

$\eta(V)$ dependence can be calculated from Eq. (10) by using the successive approximation technique in case of δ-correlated thermal current fluctuations i_f: $\langle i_f(t)i_f(t+\tau)\rangle = 2\delta(\tau)\gamma$ and $\langle i_f(t)\rangle = 0$ (t is time variable, τ is a short time interval, and time averaging is done in $\langle\ldots\rangle$). In such a way, we obtain an analytical expression for the detector response in the case of large fluctuation limit $\gamma \gg 1$, where the noise parameter γ determines the normalized bandwidth of the harmonic of Josephson oscillation γ_n (n=1,2…).

In the first order approximation in i_{rf}^2 within the MRSJ model (the terms proportional to i_{rf}^2), we obtain the following expression for the normalized amplitude of the first "integer" detector response η_1 near $V \cong V_1$ (Ref. 53)

$$\eta_1 = \frac{r_d i_{rf}^2}{8\omega^2(\omega^2\beta^2+1)}\left[\frac{\delta_1}{\delta_1^2+\gamma_1^2} - \frac{\delta_1}{\delta_1^2+(\gamma_1+1/\beta)^2}\right] + q^2 o(a^2), \quad (14)$$

where $\delta_1=\nu-\omega$ is a relative detuning of the frequency of the first harmonic of Josephson radiation ν with respect to the frequency of external radiation ω, and $r_d=R_d/R_N$ is the normalized differential resistance. It can be seen from Eq. (14) that the contribution of the second harmonic of the CPR ($|q|>1$) of the JJ to the first "integer" detector response η_1 is a small second-order term in i_{rf}^2. In contrast, the influence of the capacitance is significant and η_1 goes to zero at $\beta \gg 1$.

The form of $\eta_1(V)$ dependence significantly changes for $\beta \approx 1$ (see also Ref. 49).

For $q \neq 0$ the second-order approximation within the MRSJ model can be used to calculate the first "half-integer" detector response $\eta_{1/2}$ near $V \cong V_{1/2}$:[53]

$$\eta_{1/2} = \frac{q^2 i_{rf}^2 r_d}{\omega^2(\omega^2\beta^2+1)}\left[\frac{\delta_{1/2}}{\delta_{1/2}^2+\gamma_{1/2}^2} - \frac{\delta_{1/2}}{\delta_{1/2}^2+(\gamma_{1/2}+2/\beta)^2}\right], \tag{15}$$

where $\delta_{1/2}=2\nu-\omega$ is a relative detuning of the frequency of the second harmonic of Josephson radiation 2ν with respect to the frequency of external radiation ω. From Eq. (15) it is clearly seen that $\eta_{1/2}$ strongly depends on the second harmonic of the CPR (I_{c2}): $\eta_{1/2} \propto q^2$. If the fluctuation is strong enough $\gamma \gg 1/\beta$ then the ratio between the maxima of the first half-integer and integer detector responses is weakly dependent on β:

$$\frac{\eta_{1/2}^{\max}}{\eta_1^{\max}} \approx q^2(1+1/2\gamma\beta). \tag{16}$$

Thus, by making analysis of the detector response of the JJ in the case of large fluctuations, we can prove the presence of the second harmonic in the superconducting CPR of the JJ and also find q by making use of Eq. (16).

The shapes of the first integer and half-integer detector responses calculated using Eqs. (14) and (15), respectively, match the experimental data obtained for *t*-JHS #2 in case of $\gamma_{1/2}=2\gamma_1$ (see insets in Fig. 12). The deviation in the form of detector responses $\eta_1(V)$ and $\eta_{1/2}(V)$ at $\gamma_1, \gamma_{1/2} > 1$ could be due to violation of the condition $\gamma \gg 1$ used while deriving Eqs. (14) and (15). A crude evaluation of the ratio between $\eta_{1/2}^{\max}$ and $\eta_1^{\max}$ using Eqs. (12) and (13) for the first integer and half-integer Shapiro steps at small $a \ll 1$ and small fluctuations $\gamma \leq 1$ gives

$$\frac{\eta_{1/2}^{\max}}{\eta_1^{\max}} \approx 4q\left(q+\frac{2\beta}{(\beta\omega)^2+4}\right). \tag{17}$$

Note that the nonmonotonous dependence of $\eta_{1/2}^{\max}/\eta_1^{\max}$ versus frequency of the external radiation is observed in the *t*-JHSs. $|q|=0.2$ calculated from Eq. (17) using the experimental data plotted in Fig. 12 is smaller than $|q|=0.4$ determined from $I_c(a)$ dependence for the same *t*-JHS.

V. TILTED JOSEPHSON Nb/Au/YBCO HETEROSTRUCTURES: THE EFFECTS OF NONUNIFORM CURRENT DISTRIBUTION

In Sec. IV we successfully applied the MRSJ model for calculations of the superconducting CPR of lumped JJs assuming the average value of the second harmonic in the JJ. However, in our experiments we noticed a difference in the behavior of high frequency response between junctions having different sizes; a variation in the radiation-amplitude dependences of the critical current and Shapiro steps, as well as an unexpected variation in the second harmonic of CPR, q (see Figs. 8 and 10). The results cannot be explained by the MRSJ model: one does not expect a usual crossover from a lumped to a distributed current model as the junction dimensions always are considerably smaller than the Josephson penetration depth. However, the latter is defined by the average current density and due to faceting, there can be a strong local variation in magnitude and direction of currents within the junction area. Another way to express this variation is to introduce the so-called splintered vortices.

A. A model of 1D array of $0-\varphi_0$ nanojunctions

In order to explain our results we recall that our JJs can be considered as a periodic array of $S/D_{(001)}$ and $S/D_{(110)}$ nanojunctions. The ratio between the lengths of the nanojunctions is $L_{(110)}/L_{(001)} \approx 0.2$ and the period of the array is about 300 nm. The ratios between the harmonics of the nanojunctions obtained by fitting magnetic-measurement data are $I_{c1}^{(001)}/I_{c1}^{(110)}=3.3$ and $I_{c2}^{(001)}/I_{c2}^{(110)}=0.023$. Thus, the nanojunctions have different CPRs, which can be written in terms of superconducting current densities:

$$j_s^{(001)} = j_{c1}^{(001)} \sin\varphi + j_{c2}^{(001)} \sin 2\varphi \quad \text{for} \quad S/D_{(001)} - \text{contact}, \tag{18}$$

$$j_s^{(110)} = j_{c1}^{(110)} \sin\varphi + j_{c2}^{(110)} \sin 2\varphi \quad \text{for} \quad S/D_{(110)} - \text{contact}. \tag{19}$$

The critical current densities of the first harmonics of the CPR $j_{c1}^{(001)}$ and $j_{c1}^{(110)}$ of the $S/D_{(001)}$ and $S/D_{(110)}$ nanojunctions, respectively, may arise because of the nonzero *s*-wave component of YBCO superconducting order parameter and, in general, are different. However, both nanojunctions have the same sign of the first harmonic of the CPR. We assume $j_{c1}^{(001)}, j_{c1}^{(110)} > 0$ and $j_{c1}^{(001)}=j_{c1}^{(110)}=j_{c1}$ for simplicity. The amplitudes of the critical current densities of the second harmonics of the CPR in the $S/D_{(001)}$ and $S/D_{(110)}$ nanojunctions $j_{c2}^{(001)} < 0$, and $j_{c2}^{(110)} < 0$, respectively, can differ up to one order of magnitude. Following the works of Mints[27] we write the Ferrell-Prange equation $\varphi_{xx}=j_s(x)$, where $j_s(x)$ is given by Eqs. (18) and (19) as

$$j_s(x,\varphi) = j_{c1} \sin\varphi + \langle j_{c2}\rangle[1+g(x)]\sin 2\varphi, \tag{20}$$

where $\langle j_{c2}\rangle$ is the value of j_{c2} averaged over x (i.e., over $S/D_{(001)}$ and $S/D_{(110)}$ nanojunctions), and $g(x)$ is a function which describes rapid amplitude oscillations of the second harmonics of the CPR of the JJs. We assume that $|g(x)| \gg 1$ since $j_{c2}^{(001)} < j_{c2}^{(110)}$. The typical period of the oscillation is determined by the characteristic size of the nanojunction (characteristic length of faceting is around 300 nm). In such way we can write the phase $\varphi(x)$ as a sum of $\psi(x)$ and $\xi(x)$, which describe slow and rapid oscillations on the nanojunction length scale, respectively. $\xi(x) \ll 1$ in the *t*-JHSs, where the typical nanojunction length $b \ll \lambda_J$ and electrical current is homogeneously distributed across the nanojunction. By rewriting independent Ferrell-Prange equations for $\psi(x)$ and $\xi(x)$ terms, we obtain

$$\psi'' = j_{c1} \sin\psi + \langle j_{c2}\rangle[\sin\psi + 2\cos 2\psi\langle\xi(x)g(x)\rangle], \tag{21}$$

$$\xi'' = j_{c1}\cos(\psi)\xi + \langle j_{c2}\rangle[g(x)\sin 2\psi + 2\xi\cos 2\psi]. \tag{22}$$

By using Fourier components g_k instead of $g(x)$ and neglecting the small rapidly oscillating terms (proportional to ξ) in the right hand sides of Eqs. (21) and (22), the solution of Eq. (22) for fast phase variations can be found as

$$\xi(x) = \frac{\sin 2\psi}{2\pi} \int \frac{g_k \exp(ikx)}{k^2} dk = -\xi_g(x) \sin 2\psi, \quad (23)$$

where $\xi_g(x)$ is the Fourier component of $\xi(x)$ with a weight coefficient of k^2. Since $k \propto 1/b$, then $\xi \propto \sin(2\psi) b^2 g(x)$, i.e., $\xi \ll 1$ if $|g(x)| \ll 1/b^2$—the condition of applicability of our approach. From Eq. (23) we find

$$\langle g(x)\xi(x)\rangle = -\langle \xi_g(x) g(x)\rangle \sin 2\psi. \quad (24)$$

Therefore, Eq. (21) for slow component ψ can be rewritten as

$$\psi'' = j_{c1} \sin \psi + \langle j_{c2}\rangle \sin 2\psi - \langle j_{c2}\rangle \varepsilon \sin 4\psi, \quad (25)$$

where $\varepsilon = \langle \xi_g(x) g(x)\rangle$.

From Eq. (25) we can see that the fast spatial oscillations of the second harmonic of the CPR result in the negative fourth harmonic of the slowly varying Josephson phase. Since modulation of j_{c2} is small in the investigated JHS ($\varepsilon \ll 1$), the contribution of the fourth harmonic of the CPR has not been observed experimentally in the investigated JHS and can be neglected.

B. Splintered vortices in the tilted Nb/Au/YBCO Josephson junctions

If no fourth phase harmonic in Eq. (25) is taken into account, the equation is similar to Eq. (15) of Ref. 27, where existence of trapped unquantized magnetic vortices (splintered vortices) has been demonstrated in the JJ with alternating critical current density. Similarly to Ref. 27, large negative second harmonic of the CPR of the JJ ($|q| > 0.5$) may result in a pair of the splintered vortices $\Phi_1 < \Phi_0/2$ and $\Phi_2 > \Phi_0/2$ ($\Phi_1 + \Phi_2 = \Phi_0$) of the size λ_s. Size of the splintered vortex λ_s presents a new characteristic scale of the crossover from lumped to a distributed JJ, that is, in general, different from λ_J. λ_s has also a meaning of an effective magnetic-field penetration depth in the JJ with the finite second harmonic of the CPR and depends on q.[13] In the case of $|q| < 0.5$ the JJ has only one stable state ($\varphi = 0$) and the superconducting critical current is a single-valued function of q and corresponds to the escape of the phase from this stable state over a potential barrier.[13] At $|q| \leq 0.5$ the JJ has two degenerate stable states $\varphi = \pm\varphi_0 = \pm \arccos(1/2q)$ (see Fig. 6), and the phase can change either from $+\varphi_0$ to $2\pi - \varphi$ or from $-\varphi_0$ to $+\varphi_0$, resulting in two superconducting critical currents $j_c^{\min}$ and $j_c^{\max}$, respectively. Similarly, these two different critical currents arise at $q > 0.5$, where the JJ has 0 and π stable states.

In our experiment we were not able to distinguish between $j_c^{\max}$ and $j_c^{\min}$. For instance, we are not able to conclude if the experimentally measured j_c for the t-JHS #2 with $|q| = 0.9$ corresponds to either $j_c^{\max}$ or $j_c^{\min}$. Assuming that for t-JHS #2 $j_c = j_c^{\min}$ and using Eqs. (9) and (23) and Eq. (57) of Ref. 13, we can estimate $\lambda_s \approx 50$ μm, which is about two times smaller than the value of Josephson penetration depth $\lambda_J \approx 100$ μm, calculated from the experimentally measured superconducting critical current using Eq. (9). $\lambda_s \approx 50$ μm is still two to three times larger than the t-JHS size, where the crossover from a lumped to a distributed current model has been observed: the microwave and magnetic properties of the t-JHSs are different in the lumped and distributed limits (see Figs. 8 and 10).

The above estimations, where the large second harmonic of the CPR of the t-JHSs is taken into account cannot explain the observed crossover in the t-JHSs behavior because of several possible reasons: (i) The assumption $j_{c1}^{(001)} = j_{c1}^{(110)}$ used in Sec. V A may not be valid for the t-JHSs; (ii) The q values were calculated using Eq. (12), where no $j_c^{\max}(q)$ and $j_c^{\min}(q)$ were taken into account; (iii) The amplitudes of the superconducting critical current and integer Shapiro steps in Eq. (12) were normalized by the experimentally measured value of I_c assuming that $|q| \ll 1$ and $I_{c1} \approx I_c$; (iv) Equation (12) is rigorously valid for lumped JJ. However, the magnetic and high-frequency dynamical properties of the investigated larger Nb/Au/YBCO t-JHS deviate from the lumped JJ limit. Thus, in order to unambiguously determine q for the larger Nb/Au/YBCO t-JHS, a distributed junction approach has to be used; (v) It might be the case that the variations of the second harmonic of individual $S/D_{(001)}$ and $S/D_{(110)}$ nanojunctions are not well approximated by Eq. (19): the contribution of the second harmonic to the CPR is different for every nanojunction and, therefore, varies across the t-JHS area. (vi) Contributions of edge effects and 2D faceting geometry of the investigated planar Nb/Au/YBCO JHSs should be included into the model of $0-\varphi_0$ nanojunctions in order to obtain quantitative agreement with the experimental data.

However, the model of 1D array of $0-\varphi_0$ nanojunctions qualitatively explains the crossover from a lumped to a distributed JJ experimentally observed in the Nb/Au/YBCO t-JHSs with sizes smaller than λ_J.

Note, that in our analysis we have used the experimental evidence of the second harmonic of the CPR in the investigated Nb/Au/YBCO JHSs and suggested that it originates from the d-wave symmetry of the order parameter of YBCO. As it was mentioned in Sec. I, the second harmonic may also arise in the CPR of the JJ with sign of the first harmonic of the CPR alternating at the neighbor interface facets.[27] However, the latter mechanism of second-harmonics generation is not capable of explaining the experimentally observed relatively high negative values of the second harmonic of the CPR in the JHSs smaller than λ_s, and, thus, can be ruled out (see also Ref. 21).

VI. CONCLUSION

We investigated dynamic properties of Nb/Au/YBCO Josephson heterostructures fabricated on (001) and (1 1 20) YBCO films, where crystallographic c axis is inclined from the substrate normal direction in the latter case. Fractional Shapiro steps have been observed in the I-V curves of the JHSs irradiated by electromagnetic waves at 36–100 GHz. Dependences of the critical current and first Shapiro steps versus amplitude of electromagnetic radiation have nonzero

minima. Owing to nanofaceting of the Au/YBCO(1 1 20) interface and to the *d*-wave symmetry of the superconducting order parameter in YBCO, the investigated JHSs can be considered as arrays of parallel 0 and φ_0 nanojunctions. The nanojunctions have nonzero second harmonics of the superconducting current-phase relation. This may result in a formation of splintered vortices carrying fractional magnetic-flux quanta for experimental conditions. Thus, even if the *t*-JHS is in the lumped-junction limit, i.e., the size of the *t*-JHS is smaller in comparison to the Josephson penetration depth calculated from the average critical current density j_c, the splintered vortices might penetrate into the *t*-JHS and influence its magnetic and high-frequency properties. The presence of splintered vortices is indirectly indicated by the observed deviations of $I_c(H)$ dependence from the Fraunhofer shape. Numerical calculations with a complex-coordinate-dependent CPR are required to quantitatively simulate the experimental data.

ACKNOWLEDGMENTS

The authors thank I. M. Kotelyankii for substrate fabrication, I. Bdikin and P. Mozhaev for x-ray diffraction analysis of the YBCO films, E. Il'ichev, M. Grajcar, and R. Hlubina for SQUID measurements and theoretical calculations of superconducting current-phase relations of the Josephson junctions, and T. Y. Karminskaya for an analytical simulation of the Josephson junctions. The work was supported by AQDJJ and THIOX ESF programs, The Swedish Royal Academy of Sciences, SSF "Oxide" and SIG programs, EU Project No. NMP3-CT-2006-033191, ISTC N3743, Scientific School 54.2008.2, RFBR 08-02-00487, and the projects of the Russian Academy of Sciences.

*komissinskiy@oxide.tu-darmstadt.de

[1] C. C. Tsuei and J. R. Kirtley, Rev. Mod. Phys. **72**, 969 (2000).
[2] H. Hilgenkamp and J. Mannhart, Rev. Mod. Phys. **74**, 485 (2002).
[3] T. Löfwander, V. S. Shumeiko, and G. Wendin, Supercond. Sci. Technol. **14**, R53 (2001).
[4] L. B. Ioffe, V. B. Geshkenbein, M. V. Feigel'man, A. F. Fauchère, and G. Blatter, Nature (London) **398**, 679 (1999).
[5] H. J. H. Smilde, H. Hilgenkamp, G. J. Gerritsma, D. H. A. Blank, and H. Rogalla, Physica C **350**, 269 (2001).
[6] T. Ortlepp, Ariando, O. Mielke, C. J. M. Verwijs, K. F. K. Foo, H. Rogalla, F. H. Uhlmann, and H. Hilgenkamp, Science **312**, 1495 (2006).
[7] A. Blais and A. M. Zagoskin, Phys. Rev. A **61**, 042308 (2000).
[8] T. Bauch, T. Lindström, F. Tafuri, G. Rotoli, P. Delsing, T. Claeson, and F. Lombardi, Science **311**, 57 (2006).
[9] H. J. H. Smilde, Ariando, D. H. A. Blank, G. J. Gerritsma, H. Hilgenkamp, and H. Rogalla, Phys. Rev. Lett. **88**, 057004 (2002).
[10] S. Kashiwaya and Y. Tanaka, Rep. Prog. Phys. **63**, 1641 (2000).
[11] R. A. Riedel and P. F. Bagwell, Phys. Rev. B **57**, 6084 (1998).
[12] Yu. S. Barash, Phys. Rev. B **61**, 678 (2000).
[13] E. Goldobin, D. Koelle, R. Kleiner, and A. Buzdin, Phys. Rev. B **76**, 224523 (2007).
[14] M. H. S. Amin, A. N. Omelyanchouk, S. N. Rashkeev, M. Coury, and A. M. Zagoskin, Physica B (Amsterdam) **318**, 162 (2002).
[15] L. H. Greene, P. Hentges, H. Aubin, M. Aprili, E. Badica, M. Covington, M. M. Pafford, G. Westwood, W. G. Klemperer, S. Jian, and D. G. Hinks, Physica C **387**, 162 (2003).
[16] P. V. Komissinski, G. A. Ovsyannikov, Yu. V. Kislinskii, I. M. Kotelyanskiĭ, and Z. G. Ivanov, JETP **95**, 1074 (2002).
[17] E. Il'ichev, V. Zakosarenko, R. P. J. Ijsselsteijn, V. Schultze, H.-G. Meyer, H. E. Hoenig, H. Hilgenkamp, and J. Mannhart, Phys. Rev. Lett. **81**, 894 (1998).
[18] E. Il'ichev, M. Grajcar, R. Hlubina, R. P. J. IJsselsteijn, H. E. Hoenig, H. G. Meyer, A. Golubov, M. H. S. Amin, A. M. Zagoskin, A. N. Omelyanchouk, and M. Y. Kupriyanov, Phys. Rev. Lett. **86**, 5369 (2001).
[19] T. Lindström, S. A. Charlebois, A. Ya. Tzalenchuk, Z. Ivanov, M. H. S. Amin, and A. M. Zagoskin, Phys. Rev. Lett. **90**, 117002 (2003).
[20] P. B. Mozhaev, I. V. Borisenko, E. G. Ovsyannikova, and G. A. Ovsyannikov, Physica C **372-376**, 150 (2002).
[21] P. V. Komissinski, E. Il'ichev, G. A. Ovsyannikov, S. A. Kovtonyuk, M. Grajcar, R. Hlubina, Z. Ivanov, Y. Tanaka, N. Yoshida, and S. Kashiwaya, Europhys. Lett. **57**, 585 (2002).
[22] P. V. Komissinskii, G. A. Ovsyannikov, E. Il'ichev, and Z. Ivanov, JETP Lett. **73**, 361 (2001).
[23] P. Komissinskiy, G. A. Ovsyannikov, I. V. Borisenko, Yu. V. Kislinskii, K. Y. Constantinian, A. V. Zaitsev, and D. Winkler, Phys. Rev. Lett. **99**, 017004 (2007).
[24] A. G. Sun, D. A. Gajewski, M. B. Maple, and R. C. Dynes, Phys. Rev. Lett. **72**, 2267 (1994).
[25] R. Kleiner, A. S. Katz, A. G. Sun, R. Summer, D. A. Gajewski, S. H. Han, S. I. Woods, E. Dantsker, B. Chen, K. Char, M. B. Maple, R. C. Dynes, and J. Clarke, Phys. Rev. Lett. **76**, 2161 (1996).
[26] K. A. Kouznetsov, A. G. Sun, B. Chen, A. S. Katz, S. R. Bahcall, J. Clarke, R. C. Dynes, D. A. Gajewski, S. H. Han, M. B. Maple, J. Giapintzakis, J.-T. Kim, and D. M. Ginsberg, Phys. Rev. Lett. **79**, 3050 (1997).
[27] R. G. Mints, Phys. Rev. B **57**, R3221 (1998).
[28] R. G. Mints, I. Papiashvili, J. R. Kirtley, H. Hilgenkamp, G. Hammerl, and J. Mannhart, Phys. Rev. Lett. **89**, 067004 (2002).
[29] K. Buckenmaier, T. Gaber, M. Siegel, D. Koelle, R. Kleiner, and E. Goldobin, Phys. Rev. Lett. **98**, 117006 (2007).
[30] M. Weides, M. Kemmler, E. Goldobin, H. Kohlstedt, R. Waser, D. Koelle, and R. Kleiner, Phys. Rev. Lett. **97**, 247001 (2006).
[31] [010]YBCO∥[001]$NdGaO_3$ and [100]YBCO∥[001]$NdGaO_3$ in-plane epitaxial relations are valid if twinning occurs in the *ab* plane of the YBCO films.
[32] I. K. Bdikin, P. B. Mozhaev, G. A. Ovsyannikov, P. V. Komissinski, and I. M. Kotelyanskii, Physica C **377**, 26 (2002).
[33] I. K. Bdikin, P. B. Mozhaev, G. A. Ovsyannikov, F. V. Komissinskii, I. M. Kotelyanskiĭ, and E. I. Raksha, Phys. Solid State **43**,

1611 (2001).
[34] Yu. Ya. Divin, U. Poppe, J.-W. Seo, B. Kabius, and K. Urban, Physica C **235-240**, 675 (1994).
[35] T. Usagawa, J. Wen, T. Utagawa, S. Koyama, and Y. Enomoto, Physica C **340**, 269 (2000).
[36] F. V. Komissinskii, G. A. Ovsyannikov, and Z. G. Ivanov, Phys. Solid State **43**, 801 (2001).
[37] M. Fogelström, D. Rainer, and J. A. Sauls, Phys. Rev. Lett. **79**, 281 (1997).
[38] M. B. Walker and P. Pairor, Physica C **341-348**, 1523 (2000).
[39] G. E. Blonder, M. Tinkham, and T. M. Klapwijk, Phys. Rev. B **25**, 4515 (1982).
[40] A. V. Zaitsev, Sov. Phys. JETP **59**, 1015 (1984).
[41] M. Yu. Kupriyanov and K. K. Likharev, IEEE Trans. Magn. **27**, 2460 (1991).
[42] P. G. de Gennes, *Superconductivity of Metals and Alloys* (Westview, Colorado, 1999).
[43] J. Yoshida, T. Hashimoto, S. Inoue, Y. Mizutani, M. Sagoi, and K. Mizushima, Jpn. J. Appl. Phys., Part 1. **31** 1771 (1992).
[44] K. Krishana, J. M. Harris, and N. P. Ong, Phys. Rev. Lett. **75**, 3529 (1995).
[45] L. N. Bulaevskii, V. L. Ginzburg, and A. A. Sobyanin, Sov. Phys. JETP **68**, 1499 (1988).
[46] R. Haslinger and R. Joynt, J. Phys.: Condens. Matter **12**, 8179 (2000).
[47] M. Sigrist, K. Kuboki, P. A. Lee, A. J. Millis, and T. M. Rice, Phys. Rev. B **53**, 2835 (1996).
[48] G. A. Ovsyannikov, P. V. Komissinski, Yu. V. Kislinski, and Z. G. Ivanov, Mod. Phys. Lett. B **17**, 569 (2003).
[49] K. K. Likharev, *Dynamics of Josephson Junctions and Circuits* (Gordon and Breach, New York, 1986).
[50] A. Barone and G. Paterno, *Physics and Applications of the Josephson Effect* (Wiley, New York, 1982).
[51] T. Lindström, J. Johansson, T. Bauch, E. Stepantsov, F. Lombardi, and S. A. Charlebois, Phys. Rev. B **74**, 014503 (2006).
[52] Yu. V. Kislinskii, P. V. Komissinski, K. Y. Constantinian, G. A. Ovsyannikov, T. Yu. Karminskaya, I. I. Soloviev, and V. K. Kornev, JETP **101**, 494 (2005).
[53] G. A. Ovsyannikov, K. Y. Constantinian, Yu. V. Kislinskii, P. V. Komissinskii, I. V. Borisenko, T. Yu. Karminskaya, and V. K. Kornev, J. Commun. Technol. Electron. **51**, 1078 (2006).
[54] V. N. Gubankov, V. P. Koshelets, and G. A. Ovsyannikov, Sov. Phys. JETP **71**, 348 (1976).